Changes in Tropical Clouds and Atmospheric Circulation Associated with Rapid Adjustment Induced by Increased Atmospheric CO_2 – A Multiscale Modeling Framework Study

Kuan-Man Xu[1], Zhujun Li[2], Anning Cheng[3], Yongxiang Hu[1]

[1]Climate Science Branch, NASA Langley Research Center, Hampton, VA

[2]NASA Postdoctoral Program, Universities Space Research Association, Hampton, VA

[3]NOAA EMC/NCEP, College Park, MD

Corresponding author address:

Dr. Kuan-Man Xu

NASA Langley Research Center

Climate Science Branch

Mail Stop 420

Hampton, VA 23681

E-mail: Kuan-Man.Xu@nasa.gov

Tel: (757) 864-8564

ORCID ID is 0000-0001-7851-2629

Abstract

The radiative heating increase due to increased CO_2 concentration is the primary source for the rapid adjustment of atmospheric circulation and clouds. In this study, we investigate the rapid adjustment resulting from doubling of CO_2 and its physical mechanism using a multiscale modeling framework (MMF). The MMF includes an advanced higher-order turbulence closure in its cloud-resolving model component and simulates realistic shallow and deep cloud climatology and boundary layer turbulence. The rapid adjustment over the tropics is characterized by 1) reduced ascent and descent strengths over the ocean, 2) increased lower tropospheric stability (LTS) over the subsidence region, 3) shoaling of planetary boundary layers over the ocean, 4) increased deep convection over lands and shift of cloud coverage from the ocean to lands, and 5) reduced sensible (SH) and latent heat (LH) fluxes over the oceanic deep convective regions. Unlike conventional general circulation models and another MMF, a reduction in the global-mean shortwave cloud radiative cooling is not simulated, due to the increase in low clouds at lower altitudes over the ocean, resulting from reduced cloud-top entrainment due to strengthened inversion. Changes in regional circulation play a key role in cloud changes and shift of cloud coverage to lands. Weaker energy transport resulting from water vapor and cloud CO_2 masking effects reduces the upward motion and convective clouds in the oceanic regions. The ocean-land transports are linked to the partitioning of surface SH and LH fluxes that increases humidity over lands and enhances deep convection over the tropical lands.

Keywords: Rapid atmospheric adjustment . Tropical cloud changes . Rapid adjustment mechanism . Low-level clouds . Increased atmospheric CO_2 . Multiscale modeling framework

1 Introduction

The climate response to increased CO_2 concentration in the atmosphere involves direct and indirect effects; the direct effect is rapid adjustments to increased radiative heating while the indirect effect is the slow response to the CO_2-caused change of surface air temperature (SAT) (e.g., Andrews et al. 2010). The slow response is also referred to as the “temperature mediated” change. Rapid adjustments act in a time scale of days and weeks, which is much shorter than that of the slow response (Dong et al. 2009; Kamae and Watanabe 2012; Bony et al. 2013). As long as the CO_2 concentration continues to rise, rapid adjustments will be a crucial contributor to the climate change. It is important to understand rapid adjustments separately from slow response because the changes due to rapid adjustments are often of opposite sign from those of the slow response (e.g., Yang et al. 2003; Andrews et al. 2010; Bony et al. 2013; Sherwood et al. 2015). For example, the global-mean precipitation decreases due to abrupt CO_2 increase but it increases over the following years as the global-mean SAT increases in coupled ocean-atmosphere general circulation model (GCM) simulations.

Changes in the atmospheric thermodynamic structure and regional circulation in response to increased CO_2 concentration can cause changes in clouds and the associated changes in the cloud radiative effects (CREs) at the top of the atmosphere (TOA). CREs are defined as the differences in radiative fluxes between the clear and all skies. Zelinka et al. (2013) found that the global-mean CRE change is ~0.5 W m^{-2} from doubling of CO_2 concentration in five GCM simulations with prescribed sea surface temperature (SST), primarily from shortwave radiation. However, the signs of CRE change vary among GCMs (Gregory and Webb 2008; Webb et al. 2013). The reason for the uncertainty in the global-mean CRE change is due to the uncertainty of rapid cloud response, especially the response of low-level clouds (Andrews et al. 2012). The diversity in the lower-tropospheric specific humidity due to changes in the regional atmospheric circulations can explain most of the spreads in rapid cloud response and the associated CRE change among GCMs (Kamae and Watanabe 2012; Kamae et al. 2015).

A plausible rapid adjustment mechanism that is applicable to the tropical ocean can be described as follows. As the temperature over the oceanic regions increases in the troposphere, the lower tropospheric stability (LTS) increases while the surface turbulent heat fluxes decrease. The drying of the lower troposphere (in terms of relative humidity) reduces cloud condensate at the cloud top, while the stabilization of the lower troposphere reduces the cloud top entrainment, resulting in downshifts of the low clouds and shoaling of the planetary boundary layer (PBL) (Wyant et al. 2012; Kamae et al. 2015). A consequence of this shoaling is a reduction in shortwave (SW) cloud radiative cooling; that is, a positive change in the SW CRE in the subsidence regions of the tropics and subtropics where low clouds are abundant. However, conventional GCMs with parameterized physical processes produce diversity of low cloud simulations (Soden and Vecchi 2011; Vial et al. 2013) and thereby contribute to the uncertainty of rapid cloud adjustment and its physical mechanism.

In GCM simulations with prescribed SSTs, the global SAT cannot be held to fixed values although both SST and sea ice concentration are fixed. The smaller heat capacity of the lands allows the SAT to increase more than over the ocean due to the increased downward infrared radiation from the heated troposphere. Such temperature contrasts between the land and oceanic regions alter the regional atmospheric circulation and may shift the cloud cover at all levels from the ocean to lands, which leads to the increase of precipitation over lands (Kamae and Watanabe 2013; Wyant et al. 2012; Zelinka et al. 2013; Kamae et al. 2016; Xu et al. 2017). Although the regional circulation response to CO_2 direct radiative forcing is dominated by the CO_2 increase over lands (Shaw and Voigt 2016), the changes in surface sensible heat fluxes due to increased CO_2 concentration can also modulate changes in the regional atmospheric circulation and the hydrological cycle (Kamae et al. 2015; Shaw and Voigt 2016; Xu et al. 2017). Additionally, the plants react to increased CO_2 by closing the stomata and reducing the evapotranspiration of moisture into the atmosphere. Such a response occurs at the same time scale as cloud adjustment, therefore, should also impact the adjustment processes (Doutriaux-Boucher et al. 2009; Dong et al. 2009; Andrews et al. 2012).

The direct CO_2 radiative forcing can be weakened by the masking effect of clouds and water vapor in the deep convective regions but enhanced in the drier subtropics (Gregory and Webb 2008; Merlis 2015). The differential heating resulting from the masking effect reduces energy transport from the convective regions to the subsidence regions or higher latitudes and thus reduces the regional atmospheric circulations. The extent of the weakening of regional atmospheric circulation is related to the dependency of CO_2's radiative forcing on the climatology of clouds and humidity. Improving the representations of both shallow and deep convective cloud processes is thus important for accurately capturing such masking effects and the associated changes in regional atmospheric circulations, which can lead to a better understanding the physical mechanisms of rapid cloud responses.

The complexity of subgrid effects associated with clouds, convection, precipitation and radiation is the primary obstacle to improving model physical parameterizations in conventional GCMs (Randall et al. 2003). The multiscale modeling framework (MMF) proposed by Grabowski (2001) and Khairoutdinov and Randall (2001) is an attractive tool because it explicitly simulates the largest and most organized circulations within deep convective systems using a cloud-system resolving model (CRM) within each grid column of the global model. In the past decade, MMF has been used to perform climate change simulations (Wyant et al. 2006, 2012; Arnold et al. 2014; Bretherton et al. 2014; Stan and Xu 2014; Xu and Cheng 2016; Xu et al. 2017). The effective climate sensitivity (ECS) of MMFs is respectively 1.5 K in Wyant et al. (2006), 2.1 K in Bretherton et al. (2014) and 2.0 K in Xu and Cheng (2016) assuming a CO_2 doubling forcing of 3.7 W m^{-2} (Myhre et al. 1998), compared to 2.1-3.0 K for AMIP_4K (Atmospheric Model Intercomparison Project +4 K SST) simulations by conventional GCMs (Ringer et al. 2014).

In this study, we adopt the fixed SST approach using an MMF with an advanced higher-order turbulence closure in its CRM component (Cheng and Xu 2011; Xu and Cheng 2013a). This MMF is capable of simulating realistic shallow and deep cloud and water vapor climatology and boundary layer turbulence (Xu and Cheng 2013a, b; Cheng and Xu 2013a, b; Painemal et al. 2015). We will separately examine the rapid adjustment over the tropical lands and ocean resulting from doubling CO_2 levels except for the precipitation response. Xu et al. (2017) compared the hydrological responses to both CO_2 increase and SST perturbation for two MMFs with or without the higher-order turbulence closure. Similar to conventional GCMs, the land surface temperature in MMF may vary regionally, resulting in differential changes in regional circulation between lands and the ocean. Previous studies noticed less mid-tropospheric subsidence over the tropical lands that may allow more convection and cloud formation in the fixed SST experiments, compared to a fully coupled atmosphere-ocean GCM simulation (Andrews et al. 2012; Wyant et al. 2012). Wyant et al. (2012) analyzed cloud and circulation response of an MMF simulation to a CO_2 quadrupling, using a pair of 2-yr MMF simulations. They found a shift of cloud cover and mean ascent from ocean to land regions, with little net global change in cloud cover, and the shoaling of boundary-layer clouds in the subsidence regions (by ~80 m), which was also identified in conventional GCMs (Kamae and Watanabe 2013).

The objectives of this study are twofold: one is to understand rapid adjustments resulting from doubling of CO_2 in the MMF; and the other is to examine the rapid adjustment mechanisms operating over lands and the ocean as well as different circulation regimes over the tropical ocean. The results from this MMF will be further contrasted to those examined from conventional GCMs and a MMF with a low-order turbulence closure in its CRM component.

2 Model and experiment design

Both the fixed-SST perturbation and coupled slab-ocean (full ocean) methods have been used in conventional GCMs and MMF to study the response of clouds and atmospheric circulations to CO_2 increase (e.g., Gregory and Webb 2008; Andrews et al. 2012; Wyant et al. 2012; Bretherton et al. 2014). However, the former method is more feasible than the latter method for MMF, due to the lengthy spin-up time of an ocean model and computational cost of an MMF relative to that of a conventional GCM (Wyant et al. 2012). Both methods seem to agree on the estimated radiative forcings from the same GCM (Gregory and Webb 2008; Bala et al. 2010; Colman and McAvaney 2011; Andrews et al. 2012) although for the same method the spreads of the cloud radiative forcings are significant among GCMs (Kamae et al. 2015).

In this study, super-parameterized Community Atmosphere Model (SPCAM) MMF is used. This MMF includes an intermediately prognostic higher-order turbulence closure (IPHOC; Cheng and Xu 2006) in its CRM component, hereafter, referred to as SPCAM-IPHOC (Cheng and Xu 2011; Xu and Cheng 2013a). The host GCM is Community Atmosphere Model (CAM) version 3.5 (Collins et al. 2006). It has a horizontal grid spacing of 1.9°×2.5° and there are 32 layers in the vertical with 12 of them below 700 hPa. The high resolution below 700 hPa is used to better resolve the structures of stratocumulus clouds, compared to 6 layers below 700 hPa in the SPCAM configuration (i.e., with low-order turbulence closure in its CRM component) used in Wyant et al. (2012) and Bretherton et al. (2014). The embedded CRM is the System for Atmospheric Modeling (SAM) (Khairoutdinov and Randall 2003) with IPHOC. The CRMs have the same vertical levels as the host GCM. All CRMs have 32 grid columns with 4 km of horizontal grid spacing. Cloud microphysics and radiation are parameterized at the CRM scale. Tendencies of heat and moisture from the CRM scale communicate to the large scale via the GCM. The dynamical core provides the large-scale advective tendencies to the CRMs. The sub-CRM-scale variability is parameterized with IPHOC (Cheng and Xu 2006), as described below.

The MMF was forced by specifying climatological SST and sea ice distributions from Hadley Centre Sea Ice and Sea Surface Temperature dataset (HadISST) (Rayner et al. 2003) with monthly-mean annual cycles. The MMF simulation was integrated for 10 years and 3 months (Xu and Cheng 2013a). The results from the last nine years are analyzed in this study. This simulation is referred to as control.

In the sensitivity experiment, the CO_2 concentration of present-day climate is instantaneously doubled (Hansen et al. 1984) while the rest of experiment design are identical to those of the control experiment. As mentioned earlier, the SST and sea ice are fixed but land surface temperature is allowed to change in both experiments. This experiment was also integrated for 10 years and 3 months. As in control, the results from the last nine years are analyzed. This simulation is referred to as $2xCO_2$.

The sub-CRM-grid-scale variability is represented by IPHOC. As detailed in Cheng and Xu (2006, 2008), IPHOC assumes a joint double-Gaussian distribution of liquid water potential temperature, total water, and vertical velocity. The properties of the double-Gaussian probability density function (PDF) are determined from the first-, second-, and third-order moments of the variables given above. And the PDF is used to diagnose cloud fraction and grid-mean liquid water mixing ratio, as well as the buoyancy terms and fourth-order terms in the equations describing the evolution of the second- and third-order moments. Xu and Cheng (2013a, b), Cheng and Xu (2013a, b) and Painemal et al. (2015) extensively evaluated the control simulation described above. A major benefit of the IPHOC scheme is that the MMF is able to simulate optically thin clouds and realistic global cloud coverage and the stratocumulus in the subsidence regions as in observations. Due to its prediction of three skewness variables, shallow cumulus and its transition to stratocumulus are well simulated in this MMF. Further, the vertically-integrated water vapor is highly corrected (>0.98) with observations with a root-mean-square error less than 10% of the global mean (Xu and Cheng 2013a).

3 Results

In the results presented below, we will first discuss the geographic distributions and the global means of selected variables. We will then focus on statistics computed separately over tropical land and ocean regions (30°S-30°N), as well large-scale circulation regimes. Results from this MMF will be compared with previous studies using SPCAM (Wyant et al. 2012; Bretherton et al. 2014) and conventional GCMs with similar experimental configurations (e.g., Andrews et al. 2012; Kamae and Watanabe 2012; Zelinka et al. 2013; Kamae et al. 2015).

3.1 Global change in surface air temperature (SAT), cloud cover and cloud radiative effects

The global mean tropospheric radiative cooling rate is reduced as the CO_2 concentration doubles, especially in the middle troposphere of the Tropics between 800 and 500 hPa (Figure 1b). The global-mean SAT increases by 0.14 K as the land surfaces heat up (Figure 1a), with the tropical-land SAT increasing by 0.38 K (Table 1). The global-mean SAT increase is less than half of the values reported in similar fixed-SST MMF studies with quadrupling CO_2 concentration; 0.30 K in Wyant et al. (2012) for 2-yr runs, 0.40 K for years 2-10 and 0.49 K for years 2-30 of long integrations in Bretherton et al. (2014). The corresponding tropical-land SAT increases are 0.50 K, 0.77 K and 0.80 K. The weak sensitivity of SAT increase to the integration length after 10 years justifies the use of 10-yr integration performed in this study.

The spatial patterns of the land SAT increases are consistent with Wyant et al. (2012) and Bretherton et al. (2014); that is, the SAT increases over most continental areas except for small regions over southern/equatorial Africa, northern South America and western Australia (Figure 1a). The decrease over the Siberian region was not simulated by SPCAM, but by a conventional GCM (Andrews et al. 2012). Significant changes in regional circulation are likely responsible for these SAT decreases.

A major focus of this study is the rapid cloud adjustment. It is important to understand the vertical-horizontal distributions of cloud changes between the 2xCO_2 and control experiments. The changes in low-, middle-, high-level and total cloud amounts are shown in Figure 2. The low-level clouds are defined as those with tops between the surface and 700 hPa, middle-level clouds between 700 hPa and 400 hPa, and high-level clouds between 400 hPa and the model top. A maximum vertical overlap of cloud fractions between the chosen pressure ranges is used to obtain cloud amount for each CRM grid column. Then, cloud amounts of all CRM columns are horizontally averaged to obtain cloud amount over a GCM grid. The CRM provides cloud fraction at each CRM gridpoint from the double-Gaussian PDF.

The global-mean total cloud amount increases by 0.62%, which is contributed by both low- and high-level clouds (0.38% and 0.43%, respectively). One can see the large meridional and zonal variations of cloud amount changes with local values up to 6% (Figure 2). Most of the low-level cloud increases are contributed from the extratropical oceans (Figure 2a), which is the largest meridional variation signal. The features described below contribute to the zonal variations. The decreases of low-level cloud amount over lands such as South and North America and Europe correspond well to the SAT increases, as may be explained by the lower relative humidity (RH) due to surface temperature increase. Low-level cloud amount increases over the rest of land areas where surface temperature experiences small changes (e.g., South Asia, Africa and western Australia). A unique feature of the MMF simulations is the increase of low-level clouds over the subtropics, in particular, the southeast Pacific and southwest and northeast Atlantic Oceans, which will be further examined later. These increases also contribute to the global-mean increase, which was not simulated in SPCAM (Wyant et al. 2012; Bretherton et al. 2014) or conventional GCMs (Zelinka et al. 2013).

The global mean middle-level cloud amount decreases by 0.16%, due to the stabilization in the mid-troposphere caused by the CO_2 radiative heating (Figure 1b). This reduction is simulated in all models (e.g., Colman and McAvaney 2011; Wyant et al. 2012; Zelinka et al. 2013), but the magnitude is smaller in this MMF. This is related to the fact that middle-level cloud amount increases in some regions (Figure 2b) where there is weak large-scale vertical motion in the control experiment (Figure 3a) such as Africa (except near the Equator), southern Asia and southern Australia. The magnitudes of subsidence are reduced over the same regions in the 2xCO_2 experiment (Figure 3b), resulting in the increase of both low- and middle-level clouds (Figures 2a and 2b). This leads to an increase in albedo. But the small SAT increases over parts of these regions are likely related to the increased CO_2 masking effect (Figure 1a).

The increase of high-level cloud amount is concentrated over the latitudinal bands over the edges of the Tropics and the high latitudes. This meridional variation signal is more pronounced than that of the zonal variation. The latter is associated with the cloud increases over the land regions such as Africa, southern Asia, Australia and equatorial South America (Figure 2c), which are well correlated with the increases in upward vertical motion (Figure 3). The zonal and meridional variations can be explained by circulation changes resulting from CO_2 and water vapor masking effects. These effects act to oppose both the zonally symmetric Hadley circulation and zonally asymmetric Walker circulation (Merlis 2015). The energy transport from tropical convective regions to higher latitudes is reduced as the middle troposphere over the edges of the subtropics becomes warmer from the CO_2 radiative heating so that the upper troposphere is destabilized. But the transport from the land regions to the adjacent oceans increases as the land SAT increases (Figure 1a). The weaker cloud masking effects over the subtropical oceans also enhances the zonal energy transport from their adjacent lands. This, in turn, impacts the low clouds over the subtropics by lowering their tops (Wyant et al. 2012; Kamae and Watanabe 2013) but low-level cloud amount increases are also simulated in the 2xCO_2 experiment.

Before discussing the changes in CREs due to cloud adjustment, the effective radiative forcing (ERF) is examined, which is the change in net TOA downward radiative flux without any changes in global-mean SAT under the conditions of doubled CO_2 (Hansen et al. 2005). The ERF is 3.85 W m^{-2} for SPCAM-IPHOC, 3.48 W m^{-2} for SPCAM (Bretherton et al. 2014) and 3.77 ± 0.45 W m^{-2} for 13 CMIP5 (Coupled Model Intercomparison Project Phase 5) models (Kamae and Watanabe 2012), respectively. Therefore, the ERFs of both SPCAM and SPCAM-IPHOC lie within the range of CMIP5 models although they differ by 0.37 W m^{-2}. As shown in Table 1, the changes in LW CRE are negative for SPCAM-IPHOC (-0.47 W m^{-2}), SPCAM (-0.88 W m^{-2}) and CMIP5 models (-0.76 ± 0.11 W m^{-2}). But the change in SW CRE for SPCAM-IPHOC has an opposite sign (-0.39 W m^{-2} vs. 0.32 W m^{-2} for SPCAM and 0.62 ± 0.24 W m^{-2} for

CMIP5 models). This result is related to the large increases in low-level clouds over the mid- and high-latitude and subtropical oceans, resulting in stronger radiative cooling. Consequently, the change in net CRE for SPCAM-IPHOC (-0.86 W m^{-2}) is more negative, compared to SPCAM (-0.56 W m^{-2}) and CMIP5 models (-0.15$\pm$0.26 W m^{-2}) (Kamae et al. 2015). A majority of CMIP5 and earlier-generation models simulated positive SW CRE changes, which were consistent with reduced low-level clouds (Gregory and Webb 2008; Kamae and Watanabe 2012).

The global-mean CRE changes contain both cloud adjustment and instantaneous cloud masking effects. Utilizing an estimate of cloud masking effects from a conventional GCM (-0.56 W m^{-2}; Andrews et al. 2012), cloud adjustment for SPCAM-IPHOC is -0.30 W m^{-2}, compared to 0.0 W m^{-2} for SPCAM. The difference in cloud adjustment between the two MMFs can largely explain the difference in ERF (0.37 W m^{-2}).

The magnitudes of local changes in SW CRE can be as large as 10 W m^{-2} while those of LW CRE can be as large as 5 W m^{-2}. The local changes in net CRE are similar to those of SW CRE except for smaller magnitudes (Figure 4). Due to decreases of total cloud amount, especially those of low-level clouds (Figures 2a and 2d), the net CRE changes are positive over South and North Americas, and parts of Europe. Increases of low-level clouds in parts of the subtropical and mid- and high-latitude oceans are associated with net CRE decreases (more cooling). As the large-scale ascent is weakened (Figure 3) and clouds (especially, low-level clouds) decrease (Figure 2), net CRE increases are simulated in tropical convective regions, where net CRE increases due to cloud adjustment can be 1-2 W m^{-2} higher than shown in Figure 4c due to strong CO_2 cloud masking effects (Andrews et al. 2012). Overall, the net CRE changes are more pronounced over lands than over the ocean due to changes in regional circulation and the associated shift of clouds from the ocean to lands (Wyant et al. 2012; Shaw and Voigt 2016).

3.2 Changes in the thermodynamic and dynamic environments

The rapid adjustment mechanism discussed in the introduction is characterized by 1) reduction in the circulation strength, 2) stabilization of the lower troposphere, 3) reduction in surface turbulent heat fluxes, 4) shoaling of the marine boundary layer and 5) reduction in SW cloud radiative cooling (Colman and McAvaney 2011; Andrew et al. 2012; Kamae and Watanabe 2012, 2013; Wyant et al. 2012; Kamae et al. 2015). A key aspect of this mechanism is the decrease in the boundary-layer/cloud top entrainment, which is contributed through strengthened trade inversion (*W*yant et al. 2012). Unlike SPCAM and conventional GCMs, the change in net CRE is negative, i.e., more cooling, in the southeast subtropical Pacific and Atlantic regions, as well as the midlatitude storm track regions (Figure 4c). And the low-level cloud amounts in these three regions increase rather than decrease in conventional GCMs (Gregory and Webb 2008; Colman and McAvaney 2011; Kamae and Watanabe 2012; Zelinka et al. 2013) except for one of the two GCMs in Watanabe et al. (2012). How much do the remaining aspects of this mechanism differ from conventional GCMs and SPCAM? To answer this question, we examine a few environmental variables, with an emphasis on the changes in three regions; i.e., the tropical and subtropical oceanic subsidence regions (Figure 3a), the tropical convective regions and the tropical lands. The changes in these variables are the primary interest although the climatology of selected variables from the control experiment is also shown in Figures 3 and 5-7.

The PBL depth/height is diagnosed from GCM grid variables based upon the bulk Richardson number (Holtslag and Boville 1993). Change in the PBL depth is affected by changes in both the stability and surface virtual heat flux. The lower tropospheric stability (LTS) is defined as the difference in potential temperature between 700 hPa and the surface (Klein and

Hartmann 1993). Over the tropical and subtropical oceanic subsidence regions, there are small decreases (and no increases anywhere) in the PBL depth, typically less than 40 m (Figure 5b). The shoaling of marine boundary layer is thus consistent with previous studies (Wyant et al. 2012; Kamae and Watanabe 2013), but the largest decreases in the PBL depth occur near the edges of the subtropics (30°S or 30°N). The decrease averaged over 30°S-30°N is ~20 m, compared to 80 m reported in Wyant et al. (2012) for quadrupling CO_2. Note that 80 m was an average over a certain LTS range. The small PBL depth decreases are accompanied by increased low-level cloud amounts (Figure 2a) and strengthened trade inversions (Figure 5d). This result can be explained by the high vertical resolution used in this MMF that reduces artificial entrainment associated with a coarse resolution and limits the jump of cloud top to a smaller height interval (Cheng et al. 2010; Xu and Cheng 2013a). The sharper inversion can lead to simulation of more stratocumulus (with lower top) than cumulus clouds over these regions.

Changes in the large-scale subsidence ($\Delta\omega$) can impact the LTS and RH through the subsidence warming (Figure 3b-d). In general, changes in ω (at 850, 700 and 500 hPa) are more variable than those of the LTS. The large-scale subsidence in the strong subsidence regions (ω_{500}) (Figure 3a), i.e., the southeast subtropical Pacific and Atlantic regions, increases slightly in the 2xCO_2 experiment but its location shifts southwestwards from the strong subsidence regions where the LTS increases (Figure 5d). The RH decreases over the subtropical low cloud regions and the edges of the subtropical oceans except for the surface (Figures 6b-d). This is directly related to the CO_2 radiative heating as cloud masking effects are weak there. Kamae and Watanabe (2012) related the intermodel (conventional GCM) differences in the SW CRE change due to rapid cloud adjustment to those in RH of the subsidence regions. However, the RH decreases do not cause a reduction in low-level cloud amount there, due perhaps to a better simulation of subgrid-scale turbulence and cloud processes within the embedded CRMs than with parameterizations in conventional GCMs, which rely on RH to parameterize cloud amount. The RH decreases are also consistent with increased surface latent heat fluxes (Figure 7d).

Over most of the tropical lands where surface sensible heat fluxes increase (Figure 7b), the PBL depths increase, up to 100 m. The exceptions are the South and central Africa, Australia and part of northwest South America where sensible heat fluxes decrease but latent heat fluxes increase (Figure 7d). The LTS decreases are due to the strong increases in the SAT discussed earlier (Figure 1a). Large-scale ascent is enhanced over most of the tropical lands. This suggests that the regional atmospheric circulation changes are an important component of rapid adjustment, agreeing with previous studies (e.g., Wyant et al. 2012; Shaw and Voigt 2016). The RH increases, except for below 700 hPa over North America and parts of South American, are associated with increased deep convection and enhanced large-scale ascent (Figure 3).

Over tropical deep convective regions (Figure 3a), neither the LTS (Figure 5b) nor the PBL depth (Figure 5d) changes much as both are more relevant measures of variability for shallow clouds than deep convection. Large-scale ascent is more likely slightly reduced than enhanced, in particular, the Indian Ocean and northwestern Pacific and western Atlantic (Figures 3b-d). Since RH changes are closely connected to $\Delta\omega$, there are more areas with decreases than increases in RH and the absolute magnitudes of RH changes increase as the height increases, as in those of $\Delta\omega$. Additionally, the LH fluxes are reduced in the convective regions to balance the decreased precipitation (Figure 7c). The LH flux change plays an important role in the hydrological sensitivity, which was discussed in Xu et al. (2017).

As discussed above, regional circulation changes are a driver for cloud adjustment and changes. A statistical description of circulation changes can be helpful. The ω_{500} PDFs for both control and $2xCO_2$ experiments show similar skewed distributions with a peak at ~ 20 hPa day^{-1} (Figure 8a). Convective regimes correspond to $\omega_{500} < 0$ whereas subsidence regimes correspond to $\omega_{500} \geq 0$. The differences in ω_{500} PDFs between the two experiments confirm the weakening of circulations discussed earlier. This is evidenced by increases in power for ω_{500} between -60 and 20 hPa day^{-1} but decreases in power for the moderate and strong subsidence regimes (ω_{500} > 20 hPa day^{-1}) and smaller decreases for the strongly convective regimes (Figure 8b). Over the tropical lands, there is a clear shift in power from the subsidence to convective regimes, which agrees with Wyant et al. (2012). Over the tropical ocean, the weakening is indicated by increases in power for the weakly convective and subsidence regimes and by decreases for the strongly convective (ω_{500} < -40 hPa day^{-1}) and subsidence (ω_{500} > 25 hPa day^{-1}) regimes. The decrease for the strong subsidence regimes was, however, not simulated by Wyant et al. (2012).

The weakening of circulations can be looked in another way. We compute the average upward ($\overline{\omega}^{\uparrow}$) and downward ($\overline{\omega}^{\downarrow}$) pressure vertical velocities at four selected levels (850, 700, 500 and 200 hPa) for the entire tropics, as well as their difference $I = \overline{\omega}^{\downarrow} - \overline{\omega}^{\uparrow}$, which represents the strength of tropical overturning circulations (Bony et al. 2013). The average changes in ascending and descending areas of the control experiment ($\Delta\overline{\omega}^{\uparrow}$and $\Delta\overline{\omega}^{\downarrow}$) are also computed (Table 3), using the monthly composite data to exclude the changes due to interannual fluctuations. The largest weakening of $\overline{\omega}^{\uparrow}$ occurs at 700 and 500 hPa, but that of $\overline{\omega}^{\downarrow}$ occurs at 850 and 700 hPa. The relative weakening, $\Delta I/I$, is similar for all four levels, ranging from 0.059 at 200 hPa to 0.064 at 700 hPa. The magnitude of the weakening over the tropical ocean is larger than that of the entire tropics (Bony et al. 2013). This is evident from Figure 8 for ω_{500}.

3.3 Rapid cloud adjustment over the tropical lands and ocean and circulation regimes

We first examine the mean properties over the tropical lands and ocean (Table 1). The mean low-, middle- and high-level cloud amounts over the tropical lands are significantly higher (0.2 to 1.6%, absolute percentage) in the $2xCO_2$ experiment compared to the control experiment, so are cloud liquid water path (LWP) and ice water path (IWP). According to the definitions of LWP and IWP, which are the vertical integrals and horizontal averages of cloud-water and cloud-ice mixing ratios, respectively, changes in cloud amount also contribute to those of LWP and IWP. Over the tropical ocean, low-level cloud amount does not change, high-level cloud amount increases (0.7%) but middle-level cloud amount decreases (-0.2%). Since both LWP and IWP decrease and the decrease in LWP (-2.1%) is larger than the amount that is attributed to the decrease in middle-level clouds, oceanic clouds are optically thinner in terms of both in-cloud LWP and IWP in the $2xCO_2$ experiment. SW cloud radiative cooling over the tropical ocean is reduced by 0.3 W m^{-2} due to optically thinner clouds, but enhanced by 0.9 W m^{-2} over the tropical lands due to the increase of total cloud amount (especially, high-level clouds) and optically thicker clouds (Table 1). LW cloud radiative heating also has opposite signs over the two regions, i.e., -0.8 W m^{-2} for the ocean and 0.5 W m^{-2} for lands, reflecting the shift of large-scale ascent and deep convection from the ocean to lands.

How well do these results compare to those of SPCAM averaged over the same 9-year period (Bretherton et al. 2014) after linearly scaling the $4xCO_2$ changes to $2xCO_2$ changes? The signs of the changes agree between the two MMFs in ω_{500}, middle-level cloud amount, LWP, IWP, precipitation, TOA and surface SW and LW radiative fluxes, SW and LW CREs and SH for the tropical lands and the tropical ocean (Table 2). The disagreement appears in low-level clouds for the tropical lands (+0.2% for SPCAM-IPHOC vs -0.5% for SPCAM), high and total cloud amounts over the tropical ocean (+0.6-0.7% for SPCAM-IPHOC vs. -0.4% for SPCAM).

This disagreement does not alter the signs of CRE and TOA and surface radiative flux changes, due to compensation of increases in cloud amount with decreases in in-cloud cloud optical depth simulated in SPCAM-IPHOC. Therefore, the results from both MMFs largely support the conceptual diagram of rapid tropical cloud changes proposed by Wyant et al. (2012).

Both MMFs have the same amount of precipitation decrease on the tropical ocean (-0.15 mm day^{-1}). But SPCAM-IPHOC simulates a larger precipitation increase over the tropical lands than SPCAM (0.14 vs. 0.06 mm day^{-1}). This suggests that convection is more strongly enhanced over lands in SPCAM-IPHOC. This result is explained by different partitioning of SH and LH flux changes (Xu et al. 2017); i.e., small increases for both in SPCAM-IPHOC versus large increase in SH but large decrease in LH in SPCAM (Table 2). DeAngelis et al. (2016) found that different SH and LH partitioning in conventional GCMs also changes the ocean-land transports and the intensity of convection over both the ocean and lands. The stronger land convection in SPCAM-IPHOC also causes appreciable differences in the magnitudes (ω_{500}, LWP, IWP, LH, SW and LW CRE, TOA SW and LW, surface LW) and the signs (low- and high-level, and total cloud amounts, SH and surface SW) of the tropical-mean changes between the two MMFs.

Next, vertical profiles of a few variables are obtained for the tropical ocean and tropical lands as in previous studies (Wyant et al. 2012; Kamae and Watanabe 2013) to further explain the rapid cloud adjustment mechanism. We also obtain the mean vertical profiles for sub-regions and circulation regimes. For the tropical lands, the desert region over Africa is separated from the rest of tropical lands due to smaller cloud masking effects there. For the tropical ocean, vertical profiles for five circulation regimes are further examined. The five circulation regimes with equal size of population (20%) are obtained, based upon the distribution of annual-mean ω_{500} of the control experiment (not shown). The ω_{500} ranges are ω_{500}< -21 hPa day^{-1} for "0%-

20%", -21 ≤ ω_{500}< -4 hPa day^{-1} for "20%-40%", -4 ≤ ω_{500} <10 hPa day^{-1} for "40%-60%", 10 ≤ ω_{500}<21 hPa day^{-1} for "60-80%" and ω_{500} ≥ 21 hPa day^{-1} for "80%-100%." The first two correspond to strongly ("0%-20%") and weakly ("20%-40%") convective regimes while the last three correspond to weak, moderate and strong subsidence regimes, respectively.

There are large contrasts in the response to doubling of CO_2 between the tropical ocean and lands (Figure 9) and between desert and non-desert regions. The potential temperature increases ($\Delta\theta$) over lands are 0.1-0.3 K higher than over the ocean while they are ~0.5 K higher over deserts than over non-deserts (Figure 9b). The maximum increase ($\Delta\theta$) over the ocean appears above the marine boundary layer top (~800 hPa) and $\Delta\theta$ decreases as the height decreases. The negative $\Delta\theta$ in the upper troposphere can be explained by a reduced meridional heat transport and less condensational heating resulting from weaker deep convection. The increased stability between the surface and ~800 hPa is consistent with the increased low-level clouds simulated in SPCAM-IPHOC (Figure 9d). Over lands, $\Delta\theta$ increases in the lower troposphere (0.2-0.8 K) are much larger than in the upper troposphere (0.1-0.2 K), especially over deserts. The increased instability over lands corresponds well with enhanced upward motion (up to -2.5 hPa day^{-1}). Over deserts, $\Delta\omega$ is "bottom heavy," which is related to the large instability increase in the lower troposphere (Figure 9b). However, the upward motion over the ocean is slightly reduced (~0.5 hPa day^{-1}), especially in the upper troposphere (Figure 9c).

Over the tropical ocean, sum of cloud water and cloud ice mixing ratios ($q_c + q_i$), i.e., in-cloud value multiplied by cloud fraction, increases over a thin layer immediately below the boundary layer top (~825 hPa) but decreases rapidly above the boundary layer top. The magnitude of the largest decrease (at 760 hPa) is twice as large as that of the largest increase (at 860 hPa). This feature is related to the shoaling of the boundary layer. The decrease associated with weakened deep convection is much smaller above 600 hPa. Conventional GCMs also show an increase of marine boundary cloud fraction at below ~900 hPa (Zelinka et al. 2013) instead of below 825 hPa in this study. This difference may be related to either stronger downward radiative heating resulted from quadrupling CO_2 or artificially strong entrainment resulted from the coarser resolution in the lower troposphere used in GCMs.

Over the tropical lands, $q_c + q_i$ increases throughout the troposphere except for the lower troposphere of deserts (Figure 9d), indicating that deep convection is mostly enhanced. Over deserts, low-level clouds are reduced, which is related to the drier lower troposphere in terms of RH (Figure 9f), but deep convection is slightly enhanced. The latter is related to the slight increases of upward motion in the upper troposphere. Over non-deserts, both RH and $q_c + q_i$ increase over the entire troposphere, indicating that both low- and high-level clouds are enhanced. In the lower troposphere, there are larger moisture increases (Figure 9e) and smaller temperature increases (Figure 9b) over non-deserts, compared to over deserts. These results are related to the efficient turbulent mixing simulated in this MMF. This is also supported by the small increases in surface LH and SH fluxes, compared to SPCAM (Table 2). Thus, SPCAM-IPHOC simulates enhanced low clouds, except for those below 980 hPa, while SPCAM simulates reduced low clouds, as the land surface warms up less over non-deserts.

Both specific humidity (Δq) and RH (ΔRH) decrease above the shoaled boundary layer top of the tropical ocean. The RH increase below the shoaled boundary layer top is likely related to reduced cloud top entrainment due to strengthened inversion. To further understand this, the RH changes (ΔRH) are partitioned into two components; i.e., one is due to temperature change, $\Delta RH(\Delta T)$, and the other due to specific humidity change, $\Delta RH(\Delta q)$, so that $\Delta RH \approx \Delta RH(\Delta T) + \Delta RH(\Delta q)$, following Kamae and Watanabe (2012). The temperature and specific humidity are set to be the values in the control experiment to calculate $\Delta RH(\Delta q)$ and $\Delta RH(\Delta T)$, respectively. As seen from Figure 9g and 9h, $\Delta RH(\Delta T)$ and $\Delta RH(\Delta q)$ over the tropical ocean have opposite signs in the vertical except between 600 and 800 hPa, with $\Delta RH(\Delta T)$ dominating in the upper troposphere and $\Delta RH(\Delta q)$ in the lower troposphere. Between 800 hPa and 600 hPa, both act to reduce RH. In contrast, vertical variations of ΔRH over lands are mostly explained by $\Delta RH(\Delta T)$ except for the middle and upper troposphere over deserts.

Figure 10c shows that the weakening of regional circulations over the tropical ocean seen from Figure 9c is achieved through a large reduction in the ascent strength of convective regimes (up to 2 hPa day^{-1}) and a small reduction in the descent strength in the low and middle troposphere of moderate and strong subsidence regimes (up to 1 hPa day^{-1}). The ascent strength in the low and middle troposphere of the strongly convective regime is reduced more greatly than that of the weakly convective regime, but the descent strength of the moderate subsidence regime is reduced more greatly than that of the strong subsidence regime.

Although the five circulation regimes have various characteristics in the changes in thermodynamic/cloud/radiative profiles between the 2xCO_2 and control experiments, the strong subsidence regime is most distinct and a major contributor to the tropical-ocean mean cloud changes (Figure 9d), for example, the increase of condensate below 800 hPa. Further, this regime has the largest stability increase between the surface and 800 hPa (Figure 10b) and the largest change in radiative heating/cooling rate, (Figure 10a) but condensate reduction is minimal above 800 hPa (Figure 10d). This result is related to the weak cloud masking effects above the PBL top. For other four regimes, reduction in condensate appears in the layer above 840 hPa, but the strongly convective regime shows the greatest reduction in the vertical extent and amount of condensate (Figure 10d). Therefore, the large condensate reduction in the tropical-mean profile between 840 and 600 hPa (Figure 9d), i.e., the shoaling of the PBL, is contributed by all regimes except for the strong subsidence regime.

Although the vertical variations of moisture changes (Figures 10e-h) resemble those of the tropical-mean changes (Figures 9e-h), the magnitudes of moisture changes have large diversity in the middle/upper troposphere (<800 hPa) among the five regimes. The moisture increases from the surface to 800 hPa are related to weakened vertical moisture transport, which may be caused by strengthened inversion (Figure 10b) and/or reduced surface evaporation (Figure 7d). Above 600 hPa, RH changes are small for all regimes except for the strong subsidence regime, due to opposite effects and temperature and moisture changes. For the strong subsidence regime, both $\Delta RH(\Delta T)$ and $\Delta RH(\Delta q)$ act to reduce RH throughout the troposphere. This is only true for the layer between 800 and 700 hPa for the other four regimes. Above 500 hPa, the magnitudes of $\Delta RH(\Delta T)$ are slightly larger than those of $\Delta RH(\Delta q)$, which are related to the monotonic increase of negative temperature changes.

4 Summary and discussions

In this study, we have investigated rapid adjustment resulting from doubling of atmospheric CO_2 concentration and its physical mechanism using a multiscale modeling framework (MMF). The MMF includes an advanced higher-order turbulence closure in its CRM component. It simulates realistic shallow and deep cloud climatology and boundary-layer turbulence, in comparison with conventional GCMs and SPCAM. This ability is important for simulating rapid adjustment because of CO_2–induced cloud and water vapor masking effects that depend on cloud climatology and their impacts on regional circulation (Merlis 2015).

Although the simulated global cloud distributions from this MMF show a decrease in middle-level cloud amount as in conventional GCMs and SPCAM, low-level cloud amount increases slightly, as opposed to decreases in conventional GCMs and SPCAM. This is due to increases over the extratropical and subtropical oceans. As in conventional GCMs, high-level cloud amount also increases, due to increases over the edges of the Tropics and several land regions. The oceanic clouds in the 2xCO_2 experiment are optically thinner than those in the control experiment. Their counterparts over lands are optically thicker. Both aspects agree with conventional GCMs. However, the increases in low-level clouds simulated in this MMF result in global-mean SW cloud radiative cooling instead of warming simulated by most conventional GCMs and SPCAM. The change in net CRE is more negative than in previous studies (Gregory and Webb 2008; Kamae et al. 2015). The cloud adjustment effect, which is the net CRE change without cloud masking effect, differs by 0.30 W m^{-2} between the two MMFs, which largely explain their difference in effective radiative forcing (ERF).

This study adds distinct contributions to the rapid adjustment mechanism from different circulation regimes. This modified mechanism based upon the results from this advanced MMF is characterized by the following elements: 1) reduced ascent and descent strengths over the ocean with the largest reduction for the strongly convective and moderate subsidence regimes, respectively, 2) increased lower tropospheric stability (in particular, between the surface and 800 hPa) over the subsidence region, which strengthens the trade inversion and reduces the entrainment despite an overall reduction in the subsidence strength, 3) shoaling of planetary boundary layers over the ocean with the largest reduction in the PBL depth away from the tropical and subtropical regions and the smallest reduction for the strong subsidence regime, 4) increased strengths of ascent and deep convection over lands and shift of cloud coverage from the ocean to lands, particularly over non-deserts, and 5) reduction in the SH and LH fluxes over the oceanic deep convective regions but small increases of both SH and LH fluxes over lands.

In this study, a decrease in the global-mean SW cloud radiative cooling is not simulated, which is a key outcome of the rapid adjustment mechanism in earlier studies with conventional GCMs and SPCAM. The shoaling of the PBL is not as pronounced as in earlier studies, in particular, over the strong subsidence regions where low-level clouds prevail. The MMF simulates an increase in low-level cloud fraction/condensate at a slightly lower altitude. This is related to the CO_2-induced radiative heating above the PBL top, which increases the stability and reduces the entrainment. This means that the embedded CRM with IPHOC more likely simulates stratocumulus clouds rather than cumulus clouds. The high vertical resolution in the lower troposphere used in this MMF also helps to reduce artificial entrainment and minimizes the extent of the PBL shoaling (Cheng et al. 2010; Xu and Cheng 2013a).

Changes in regional circulation play a key role in influencing the different cloud changes between the ocean and lands. Weaker energy transport resulting from CO_2 cloud and water vapor masking effects in the oceanic regions with strong large-scale ascent reduces the upward motion and convective clouds. Over lands, large-scale upward motion is enhanced throughout the entire troposphere, accompanied by increased moisture related to efficient turbulent mixing. Due to differences in surface warming between desert and non-desert regions, low-level clouds over non-deserts increases rather than decreases over deserts. Deep convection is also enhanced more over non-deserts. Large increases of humidity over lands are related to the land-ocean transports that are linked to the partitioning of surface SH and LH fluxes (DeAngelis et al. 2016). This MMF simulates small increases in both SH and LH over the tropical lands, compared to large increases in SH but large decreases in LH in SPCAM.

The rapid adjustment mechanism outlined in this study may need further investigation because some of the differences from previous studies may be related to nonlinearity in the responses between doubling and quadrupling of CO_2 and to the coarser vertical resolutions used in other studies. However, the MMF results presented in this study will be helpful to further advance our understanding of rapid adjustment simulated in conventional GCMs if the differences between the parameterized and explicitly simulated cloud processes can be understood.

Acknowledgments: The authors were supported by NASA Interdisciplinary Study program (Grant NNH12ZDA001N-IDS) and NASA Data for Operation and Assessment (Grant NNH16ZDA001N-NDOA). The computational resources were provided by Argonne National Laboratory, DOE's Office of Science and the local computation clusters: K-cluster and Icluster. ZL acknowledges the support of NASA Postdoctoral Program.

References

Andrews, T., P. M. Forster, O. Boucher, N. Bellouin, and A. Jones (2010), Precipitation, radiative forcing and global temperature change, *Geophys. Res. Lett., 37,* L14701, doi:10.1029/2010GL043991.

Andrews, T., J. M. Gregory, P. M. Forster, and M. J. Webb (2012), Cloud adjustment and its role in CO2 radiative forcing and climate sensitivity: A review, *Surv. Geophys.*, *33,* 619-635, doi: 10.1007/s10712-011-9152-0.

Arnold, N. P., M. Branson, M. A. Burt, D. S. Abbot, Z. Kuang, D. A. Randall, and E. Tziperman (2014), The effects of explicit atmospheric convection at high CO2, *Proc. Natl. Acad. Sci. U. S. A.*, *111*, 10,943–10,948, doi:10.1073/pnas.1407175111.

Bala, G., K. Calderia, and R. Nemani (2010), Fast versus slow response in climate change: implications for the global hydrological cycle, *Clim. Dyn. 35*, 423–34.

Bony, S., G. Bellon, D. Klocke, S. Sherwood, S. Fermepin, and S. Denvil (2013), Robust direct effect of carbon dioxide on tropical circulation and regional precipitation, *Nat. Geosci.*, *6*, 447-451, doi: 10.1038/NGEO1799.

Bretherton, C. S., P. N. Blossey, and C. Stan (2014), Cloud feedbacks on greenhouse warming in the superparameterized climate model SPCCSM4, *J. Adv. Model. Earth Syst.*, *6*, doi:10.1002/2014MS000355.

Cheng A., and K.-M. Xu (2006), Simulation of shallow cumuli and their transition to deep convective clouds by cloud-resolving models with different third-order turbulence closures, *Q. J. Roy. Meteor. Soc. 132,* 359-382.

Cheng A., and K.-M. Xu (2008), Simulation of boundary-layer cumulus and stratocumulus clouds using a cloud-resolving model with low and third-order turbulence closures, *J. Meteor. Soc. Japan, 86A*, 67-86.

Cheng, A., and K.-M. Xu (2011), Improved low-cloud simulation from a multiscale modeling framework with a third-order turbulence closure in its cloud-resolving model component, *J. Geophys. Res.*, *116*, D14101, doi:10.1029/2010JD015362.

Cheng, A., and Xu, K.-M. (2013a), Improving low-cloud simulation from an upgraded multiscale modeling framework model. Part III: Tropical and subtropical cloud transitions over the northern Pacific, *J. Climate*, *26*, 5761-5781.

Cheng, A., and Xu, K.-M. (2013b), Diurnal variability of low clouds in the southeast Pacific simulated by an upgraded multiscale modeling framework model, *J. Geophys. Res.*, *118*, 9191-9208, doi:10.1002/jgrd.50683.

Cheng, A., K.-M. Xu, and B. Stevens (2010), Effects of resolution on the simulation of boundary-layer clouds and the partition of kinetic energy to subgrid scales, *J. Adv. Model. Earth Syst.*, *2*, 3, doi:10.3894/JAMES.2010.2.3.

Collins, W. D., et al. (2006), The formulation and atmospheric simulation of the Community Atmosphere Model Version 3 (CAM3), *J. Climate*, *19*, 2144–2161.

Colman, R. A., and B. J. McAvaney (2011), On tropospheric adjustment to forcing and climate feedbacks, *Clim. Dyn.*, **36**, 1649–1658, doi:10.1007/s00382-011-1067-4.

DeAngelis, A. M., X. Qu, and A. Hall (2016), Importance of vegetation processes for model spread in the fast precipitation response to CO_2 forcing, *Geophys. Res. Lett.*, *43*, 12,550–12,559, doi:10.1002/2016GL071392.

Doutriaux-Boucher, M., M. J. Webb, J. M. Gregory, and O. Boucher (2009), Carbon dioxide induced stomatal closure increases radiative forcing via a rapid reduction in low cloud, Geophys. Res. Lett., 36, L02703, doi:10.1029/2008GL036273.

Dong, B., J. M. Gregory, and R. T. Sutton (2009), Understanding land-sea warming contrast in response to increasing greenhouse gases, Part I: Transient adjustment, *J. Clim.*, *22,* 3079-3097.

Gregory, J., and M. Webb (2008), Tropospheric adjustment induces a cloud component in CO_2 forcing, *J. Clim.*, *21*, *58–71, doi: 10.1175/2007JCLI1834.1.*

Grabowski, W. W. (2001), Coupling cloud processes with the large-scale dynamics using the cloud-resolving convection parameterization (CRCP), *J. Atmos. Sci.*, *58,* 978–997.

Hansen, J., A. Lacis, D. Rind, G. Russell, P. Stone, I. Fung, R. Ruedy, and J. Lerner (1984), Climate sensitivity: Analysis of feedback mechanisms, in *Climate Processes and Climate Sensitivity*, *Geophys. Monogr. 29,* edited by J. E. Hansen and T. Takahashi, pp. 130–163, AGU, Washington, D. C.

Hansen, J., M. Sato, R. Ruedy, and etc. (2005), Efficacy of climate forcings, *J. Geophys. Res.*, *110*, D18104, doi:10.1029/2005JD005776.

Holtslag, A. A. M., and B. A. Boville (1993), Local versus nonlocal boundary layer diffusion in a global climate model, *J. Climate*, *6*, 1825–1842.

Kamae, Y., and M. Watanabe (2012), On the robustness of tropospheric adjustment in CMIP5 models, *Geophys. Res. Lett.*, *39,* L23808, doi:10.1029/2012GL054275.

Kamae, Y., and M. Watanabe (2013), Tropospheric adjustment to increasing CO_2: Its timescale and the role of land-sea contrast, *Clim. Dyn.*, *41,* 3007-3024.

Kamae, Y., M. Watanabe, T. Ogura, M. Yoshimori, and H. Shiogama (2015), Rapid adjustments of cloud and hydrological cycle to increasing CO2: A review, *Curr. Clim. Change Rep.*, *1*, 103-113, doi: 10.1007/s40641-015-0007-5.

Kamae, Y., T. Ogura, M. Watanabe, S.-P. Xie, and H. Ueda (2016), Robust cloud feedback over tropical land in a warming climate, *J. Geophys. Res., Atmos., 121, doi:*10.1002/2015/JD024525.

Khairoutdinov, M. F., and D. A. Randall (2001), A cloud resolving model as a cloud parameterization in the NCAR community climate system model: Preliminary results. *Geophys. Res. Lett.*, *28*, 3617–3620.

Khairoutdinov, M. F., and D. A. Randall (2003), Cloud resolving modeling of the ARM summer 1997 IOP: Model formulation, results, uncertainties, and sensitivities, *J. Atmos. Sci.*, *60*, 607–625.

Klein, S. A., and D. L. Hartmann (1993), The seasonal cycle of low stratiform clouds, *J. Climate*, 6, 1587–1606.

Merlis, T. M. (2015), Direct weakening of tropical circulations from masked CO_2 radiative forcing, *Proc. Natl. Acad. Sci.*, *112*,13167–13171. Doi: 10.1073/pnas.1508268112.

Myhre, G., E. J. Highwood, K. P. Shine, and F. Stordal (1998), New estimates of radiative forcing due to well mixed greenhouse gases, *Geophys. Res. Lett. 25*, 2715-2718. Doi: 10.1029/98GL01908.

Painemal, D., K.-M. Xu, A. Cheng, P. Minnis, and R. Palikonda (2015), Mean Structure and diurnal cycle of Southeast Atlantic boundary layer clouds: Insights from satellite observations and multiscale modeling framework simulations, *J. Climate, 28*, 324-341. Doi: 10.1175/JCLI-D-14-00368.1.

Randall, D., M. Khairoutdinov, A. Arakawa, and W. W. Grabowski (2003), Breaking the cloud parameterization deadlock, *Bull. Am. Meteorol. Soc., 84*, 1547–1564.

Rayner, N. A., D. E. Parker, E. B. Horton, C. K. Folland, L. V. Alexander, D. P. Rowell, E. C. Kent, and A. Kaplan (2003), Global analyses of sea surface temperature, sea ice, and night marine air temperature since the late nineteenth century, *J. Geophys. Res., 108*, 4407, doi:10.1029/2002JD002670.

Ringer, M. A., T. Andrews, and M. J. Webb (2014), Global-mean radiative feedbacks and forcing in atmosphere-only and coupled atmosphere-ocean climate change experiments, *Geophys. Res. Lett., 41*, 4035–4042, doi:10.1002/2014GL060347.

Shaw, T. A., and A. Voigt (2016), Land dominates the regional response to CO2 direct radiative forcing, *Geophys. Res. Lett., 43*, 11,383-11,391, doi: 10.1002/2016GL071368.

Sherwood, S. C., S. Bony, O. Boucher, C. S. Bretherton, P. M. Forester, J. M. Gregory, and B. Stevens (2015), Adjustments in the forcing-feedback framework for understanding climate change, *Bull. Amer. Meteor. Soc., 96*, 217-228, doi:10.1175/BAMS-D-13-00167.1.

Soden, B. J., and G. A. Vecchi (2011), The vertical distribution of cloud feedback in coupled ocean-atmosphere models, *Geophys. Res. Lett., 38, L12704,* doi:10.1029/2011GL047632.

Stan, C., and L. Xu (2014), Climate simulations and projections with the super-parameterized CCSM4, *Environ. Model. Software, 60,* 1234-252, doi:10.1016/j.envsoft.2014.06.013.

Vial, J., J.-L. Dufresne, and S. Bony (2013), On the interpretation of inter-model spread in CMIP5 climate sensitivity estimates, *Clim. Dyn.,* 3339-3362. doi:10.1007/s00382-013—1725.9.

Watanabe, M., et al. (2012), Fast and slow timescales in the tropical low-cloud response to increasing CO_2 in two climate models, *Clim. Dyn.*, *39*, 1627–1641, doi:10.1007/s00382-011-1178-y.

Webb, M. J., F. H. Lambert, and J. M. Gregory (2013), Origins of differences in climate sensitivity, forcing and feedback in climate models, *Clim. Dyn.*, *40*, 677–707.

Wyant, M. C., M. Khairoutdinov, and C. S. Bretherton (2006), Climate sensitivity and cloud response of a GCM with a superparameterization, *Geophys. Res. Lett.*, *33*, L06714, doi:10.1029/2005GL025464.

Wyant, M. C., C. S. Bretherton, P. N. Blossey, and M. Khairoutdinov (2012), Fast cloud adjustment to increasing CO2 in a superparameterized climate model, J. Adv. Model. Earth Syst., 4, M05001, doi:10.1029/2011MS000092.

Xu, K.-M., and A. Cheng (2013a), Improving low-cloud simulation from an upgraded multiscale modeling framework model, Part I: Sensitivity to spatial resolution and climatology, *J. Climate*, *26*, 5717-5740.

Xu, K.-M., and A. Cheng (2013b), Improving low-cloud simulation from an upgraded multiscale modeling framework model, Part II: Seasonal variations over the eastern Pacific, *J. Climate*, *26*, 5741-5760.

Xu, K.-M., and A. Cheng (2016), Understanding the tropical cloud feedback from an analysis of the circulation and stability regimes simulated from an upgraded multiscale modeling framework. *J. Adv. Mod. Earth System*, *8*, 1825-1846, doi:10.1002/2016MS000767.

Xu, K.-M., Z. Li, A. Cheng, P. N. Blossey, and C. Stan (2017), Differences in the hydrological cycle and sensitivity between multiscale modeling frameworks with and without a higher-order turbulence closure, *J. Adv. Mod. Earth System*, *9*, 2120-2137, doi:10.1002/2017MS000970.

Yang, F., A. Kumar, M. E. Schlesinger, and W. Wang (2003), Intensity of hydrological cycles in warmer climates, *J. Climate*, *16*, 2419–2423.

Zelinka, M. D., S. A. Klein, K. E. Taylor, T. Andrews, M. J. Webb, J. M. Gregory, and P. M. Forster (2013), Contributions of different cloud types to feedbacks and rapid adjustment in CMIP5, *J. Clim.*, *26*, 5007–5027, doi:10.1175/JCLI-D-12-00555.1.

Table 1. The average values over the entire tropics, tropical ocean, tropical land and entire globe for the control experiment as well as the differences between the 2xCO_2 and control experiments. For ω_{500}, the percentage change is the strength of tropical overturning circulation shown in Table 3.

	Control				2×CO_2 - Control				
	Tropics			Globe	Tropics			Globe	Tropics
	Ocean	Land	Total		Ocean	Land	Total		Total %
T_s (K)	299.22	296.19	298.42	287.85	0.00	0.38	0.10	0.16	0.03
ω_{500} (hPa day^{-1})	-1.76	3.21	-0.46	0.08	0.59	-2.16	-0.13	0.00	6.02
Low cloud (%)	43.6	20.6	37.5	45.1	0.0	0.2	0.0	0.38	0.12
Middle cloud (%)	8.4	11.8	9.3	17.2	-0.2	0.4	-0.1	-0.16	-0.63
High cloud (%)	43.9	25.9	39.1	29.2	0.7	1.6	1.0	0.43	2.43
Total cloud (%)	68.3	40.5	61.0	61.7	0.6	1.2	0.7	0.62	1.21
LWP (g m^{-2})	111.4	70.5	100.7	98.2	-2.1	1.4	-1.2	0.13	-1.15
IWP (g m^{-2})	39.2	33.2	37.6	48.3	-0.3	2.5	0.5	0.11	1.21
Rain (mm day^{-1})	4.02	2.67	3.67	2.86	-0.16	0.14	-0.08	-0.06	-2.23
LHF (W m^{-2})	150.4	60.6	126.8	88.5	-2.3	0.4	-1.6	-0.95	-1.24
SHF (W m^{-2})	15.6	48.9	24.4	23.4	-0.2	0.3	-0.1	-0.11	-0.33
SW CRE (W m^{-2})	-55.8	-40.5	-51.8	-50.4	0.3	-0.9	0.0	-0.39	0.07
LW CRE (W m^{-2})	26.6	20.4	25.0	22.9	-0.8	0.5	-0.4	-0.47	-1.75
SW TOA (W m^{-2})	306.8	282.2	300.4	240.4	0.3	-0.7	0.0	-0.30	0.01
LW TOA (W m^{-2})	259.7	264.6	261.0	240.3	-3.9	-5.0	-4.2	-3.55	-1.61
SW SFC (W m^{-2})	213.9	187.3	207.0	161.8	0.1	-1.3	-0.2	-0.55	-0.12
LW SFC (W m^{-2})	55.9	78.5	61.8	57.5	-2.5	-1.5	-1.7	-1.90	-2.81

Table 2. The average differences over the entire tropics, tropical ocean and tropical lands between the xCO_2 and control experiments from the ensemble of CMIP5 models (Kamae and Watanabe 2012), SPCAM (Bretherton et al. 2014) and SPCAM-IPHOC.

	CMIP5 Ensemble			SPCAM			SPCAM-IPHOC		
	Ocean	Land	Tropics	Ocean	Land	Tropics	Ocean	Land	Tropics
ω_{500} (hPa day^{-1})	0.43	-0.96	0.08	0.60	-1.98	-0.06	0.59	-2.16	-0.13
Total cloud (%)	-0.4	-0.3	-0.4	-0.4	0.4	-0.2	0.6	1.2	0.7
Low cloud (%)				-0.1	-0.5	-0.2	0.0	0.2	0.0
Middle cloud (%)				-0.3	0.6	-0.1	-0.2	0.4	-0.1
High cloud (%)				-0.4	1.0	-0.1	0.7	1.6	1.0
LWP (g m^{-2})				-2.7	0.9	-1.8	-2.1	1.4	-1.2
IWP (g m^{-2})				-0.7	2.4	0.1	-0.3	2.5	0.5
Rain (mm day^{-1})				-0.16	0.06	-0.10	-0.16	0.14	-0.08
LHF (W m^{-2})				-2.8	-2.7	-2.8	-2.3	0.4	-1.6
SHF (W m^{-2})				-0.2	1.7	0.3	-0.2	0.3	-0.1
SW CRE (W m^{-2})	0.7	0.4	0.6	1.1	-0.8	0.6	0.3	-0.9	0.0
LW CRE (W m^{-2})	-1.1	-0.1	-0.8	-1.5	0.7	-0.9	-0.8	0.5	-0.4
SW TOA (W m^{-2})				1.1	-0.4	0.7	0.3	-0.7	0.0
LW TOA (W m^{-2})				-2.9	-5.0	-3.5	-3.9	-5.0	-4.2
SW SFC (W m^{-2})				1.1	-0.7	0.7	0.1	-1.3	-0.2
LW SFC (W m^{-2})				-1.0	-1.9	-1.2	-2.5	-1.5	-1.7

Table 3. Pressure vertical velocity (ω) and fractional area (σ) at 850, 700, 500 and 200 hPa levels for 30°S to 30°N that are obtained for different signs of vertical velocity, upward ($\overline{\omega}^{\uparrow}$, negative) and downward ($\overline{\omega}^{\downarrow}$, positive) of the control experiment. I represents the strength of tropical overturning circulation. Note that changes between the $2xCO_2$ and control experiments ($\overline{\Delta\omega}^{\uparrow}$ and $\overline{\Delta\omega}^{\downarrow}$) are calculated over the same areas with upward and downward velocity of the control experiment. The monthly composite (averaged over the same month from years 2-9) data are used to eliminate the changes due to interannual fluctuations. Unit for pressure vertical velocity is hPa day^{-1}.

	850 hPa	700 hPa	500 hPa	200 hPa
$\overline{\omega}$	-0.62	-0.65	-0.47	-0.37
$\overline{\omega}^{\downarrow}$	23.43	23.26	22.00	12.41
$\overline{\omega}^{\uparrow}$	-32.00	-33.75	-34.60	-18.35
$I = \overline{\omega}^{\downarrow} - \overline{\omega}^{\uparrow}$	55.43	57.01	56.60	30.76
$\overline{\Delta\omega}^{\downarrow}$	-1.66	-1.73	-1.49	-0.78
$\overline{\Delta\omega}^{\uparrow}$	1.70	1.91	1.92	1.05
$\Delta I = \overline{\Delta\omega}^{\downarrow} - \overline{\Delta\omega}^{\uparrow}$	-3.36	-3.64	-3.41	-1.83
$\sigma(\omega^{\downarrow})$	0.57	0.58	0.60	0.58
$\sigma(\omega^{\uparrow})$	0.44	0.42	0.40	0.42

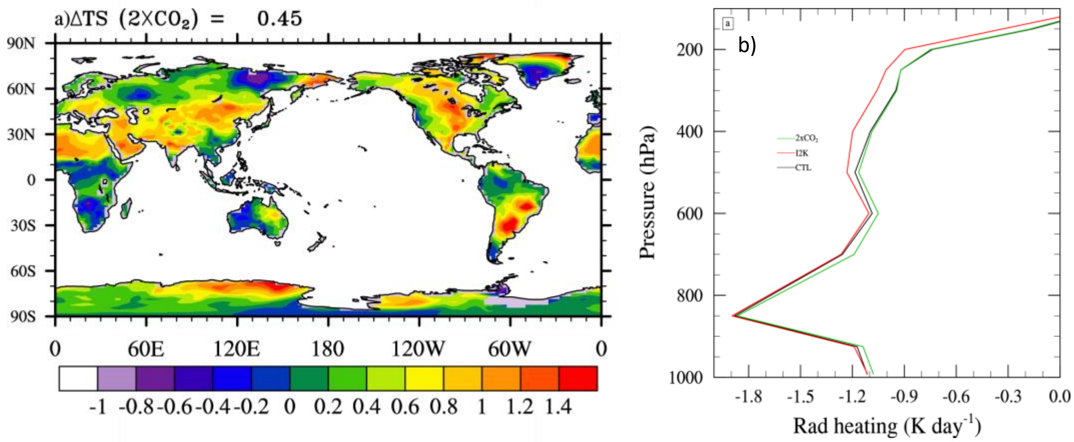

Figure 1. (a) Annual-averaged surface air temperature change between the 2xCO_2 and control experiments. (b) Annual- and tropical-mean profiles of radiative heating rates for the control (CTL; black), 2xCO_2 (green) and +2K SST (red) experiments. The +2K SST experiment is provided for reference although it is discussed in Xu and Cheng (2016) and Xu et al. (2017).

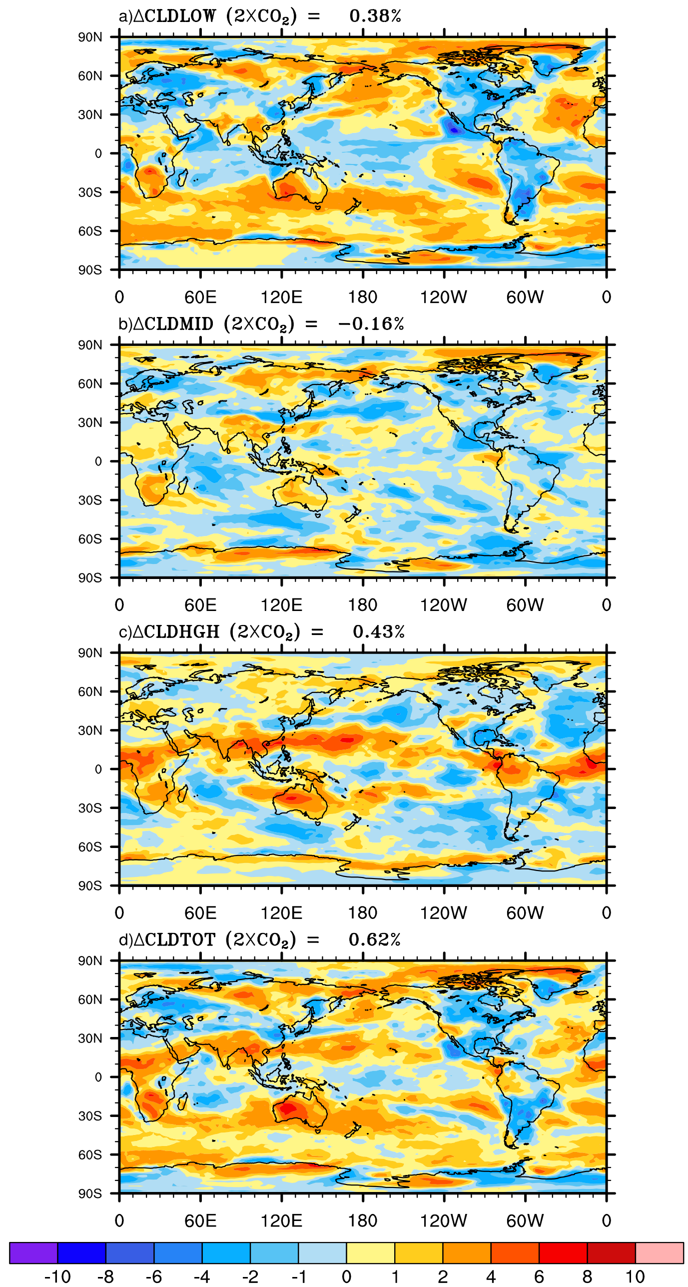

Figure 2. Annual-averaged (a) low-, (b) middle-, high-level (c) and total cloud amount changes between the $2xCO_2$ and control experiments.

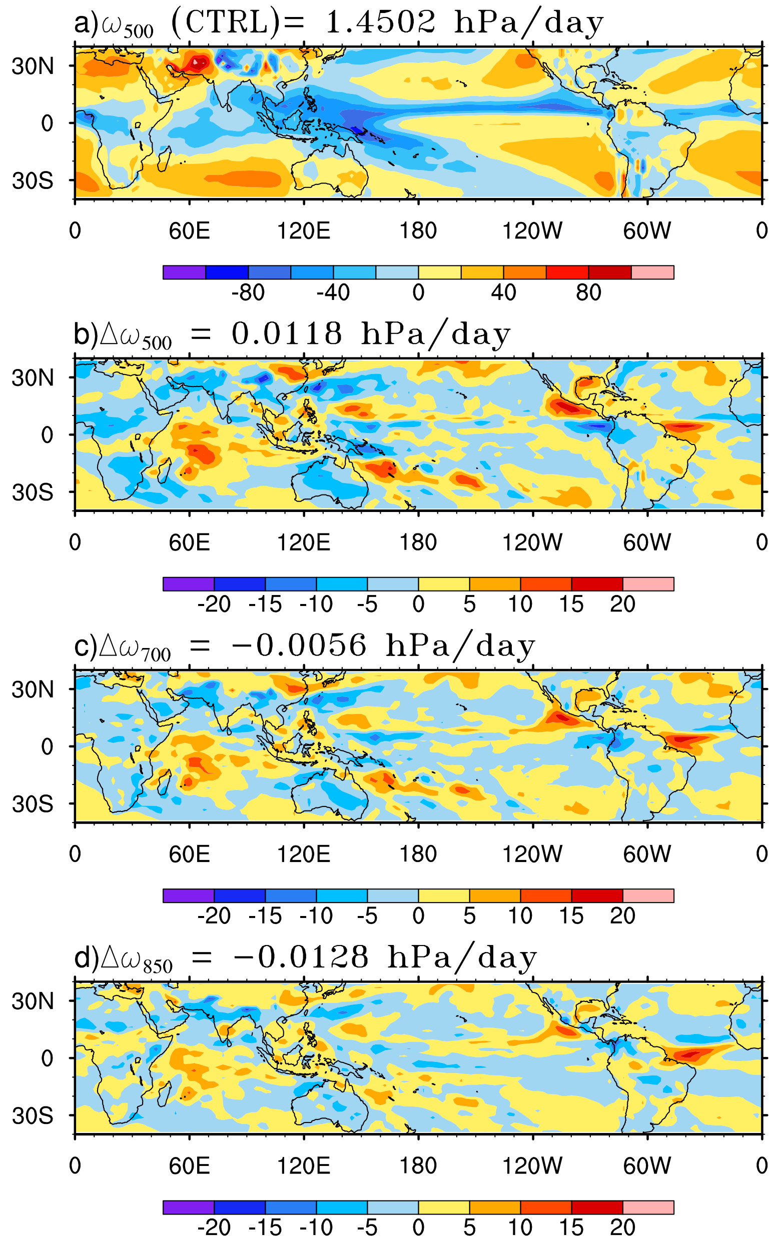

Figure 3. (a) Annual-averaged pressure vertical velocity at 500 hPa (ω_{500}) for the control experiment, and annual-averaged changes in (b) ω_{500} (c) ω_{700}, and (d) ω_{850} between the $2xCO_2$ and control experiments.

746

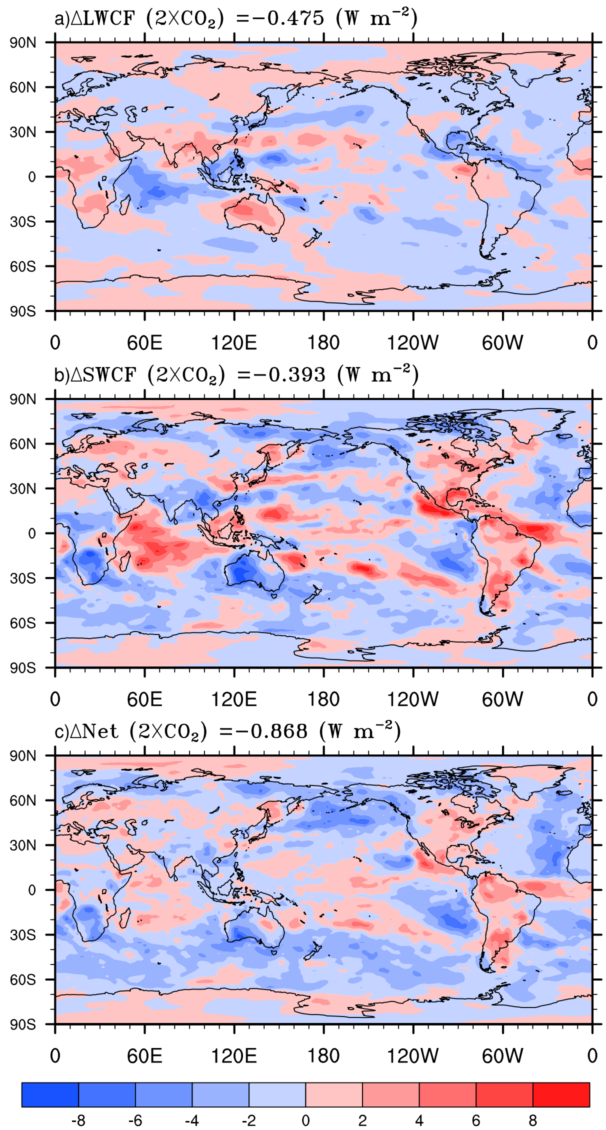

Figure 4. Annual-averaged (a) longwave, (b) shortwave and (c) net cloud radiative effect changes between the 2xCO_2 and control experiments.

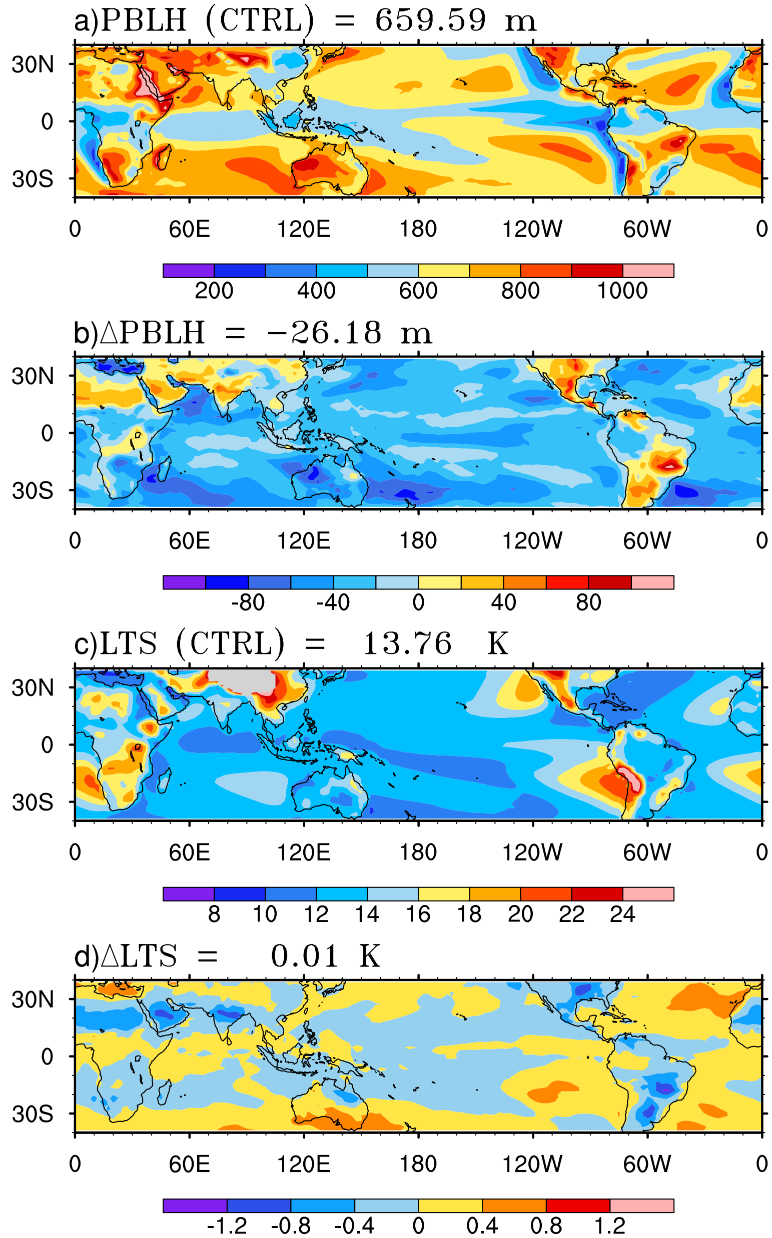

Figure 5. Annual-averaged (a) PBL height and (c) lower tropospheric stability (LTS) from the control experiment and their changes (b, d) between the $2xCO_2$ and control experiments.

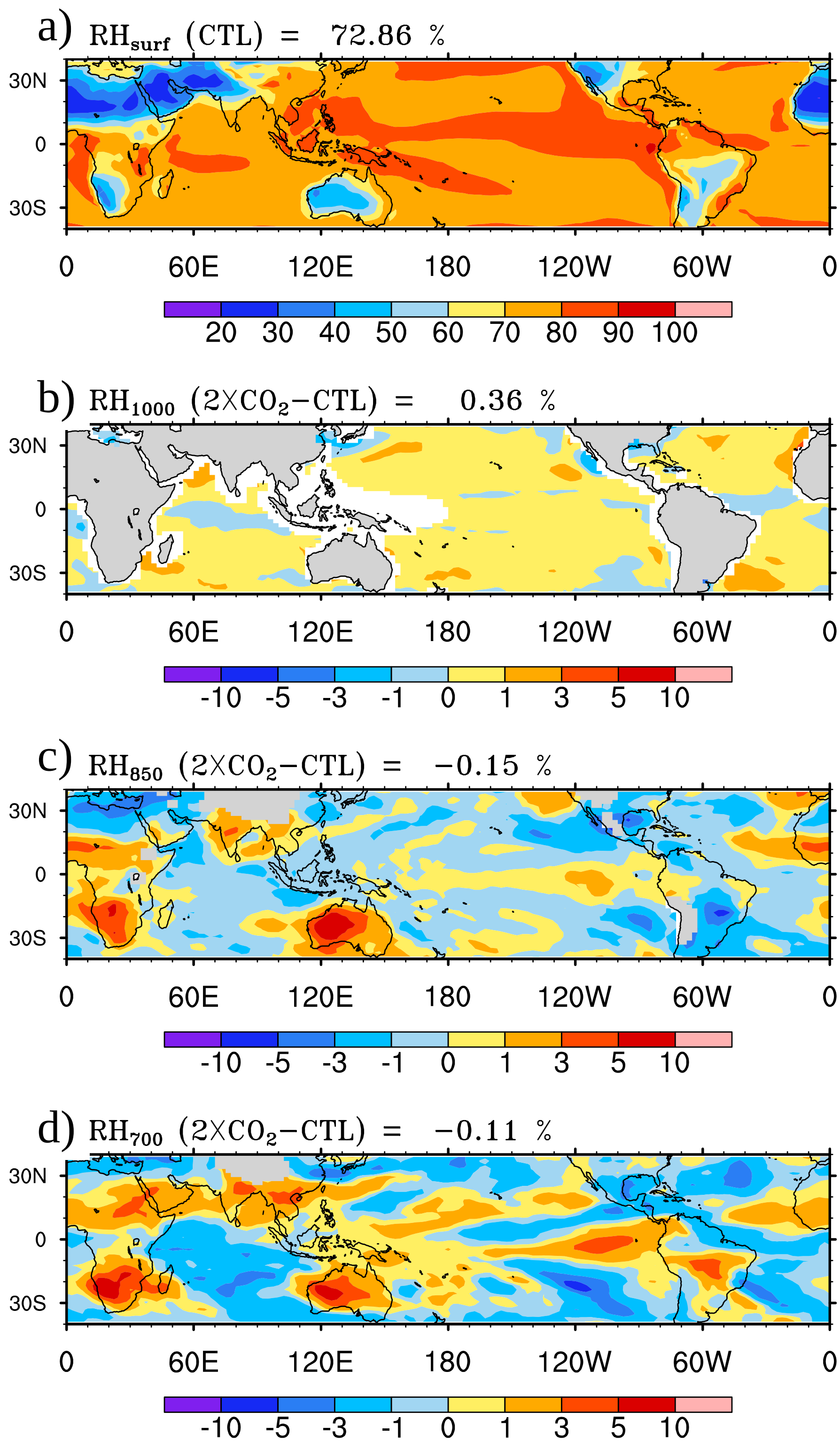

Figure 6. Annual-averaged relative humidity at first model level from the control experiment (a) and the changes at first model level (b), 850 hPa (c) and 700 hPa (d) between the $2xCO_2$ and control experiments.

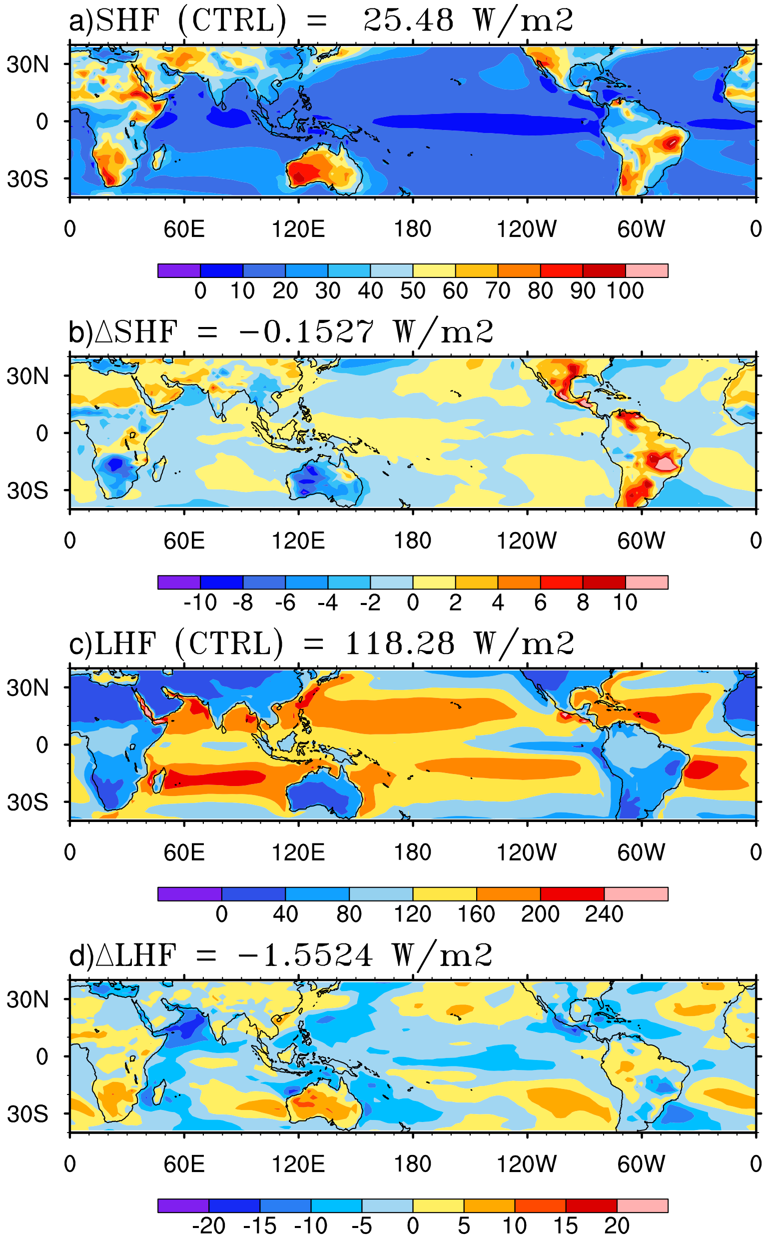

Figure 7. Annual-averaged (a) sensible heat (SH) and (c) latent heat (LH) fluxes from the control experiment and their changes (b, d) between the $2xCO_2$ and control experiments.

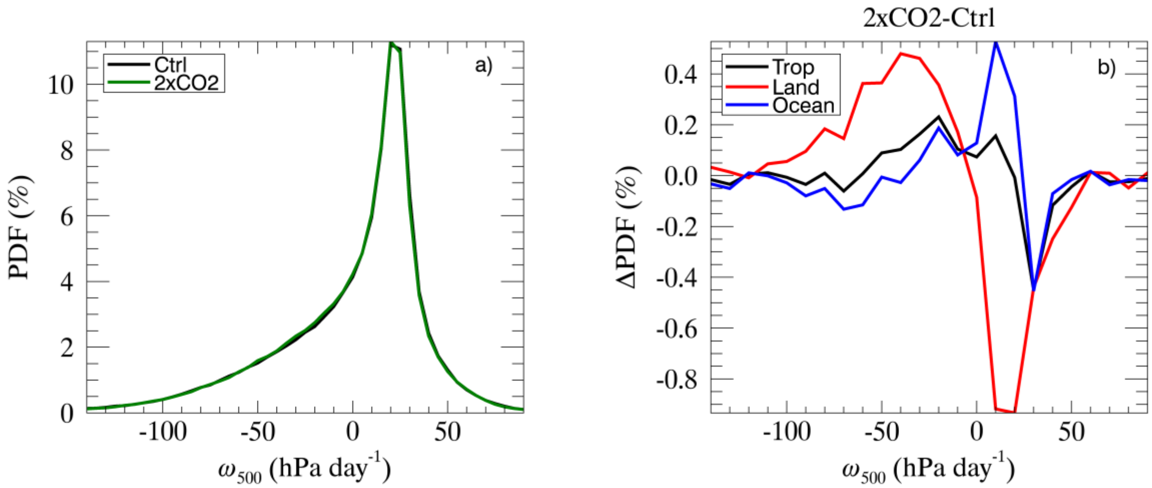

Figure 8. The frequency (%) of midtropospheric pressure velocity (ω_{500}) over the entire tropics (a) and the difference of frequency between the $2xCO_2$ and control experiments (b) for the entire tropics (black), tropical land (land) and tropical ocean (blue). The bin size is 5 hPa day^{-1}.

753

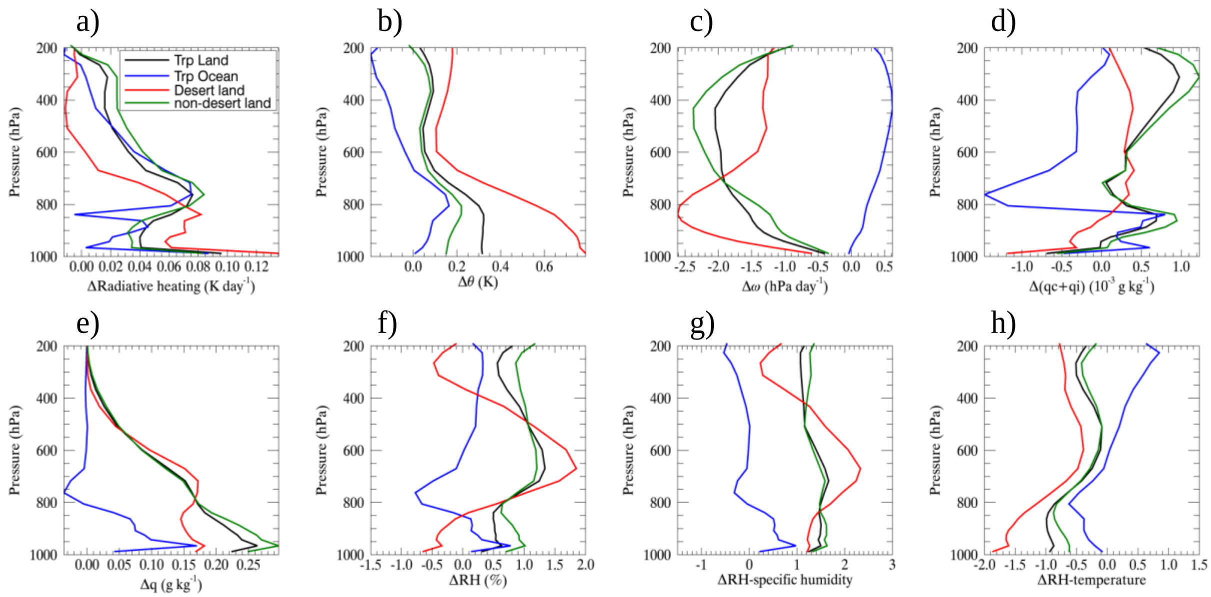

Figure 9. Vertical profiles of changes in (a) radiative heating rate, (b) potential temperature, (c) pressure vertical velocity, (d) sum of cloud water and cloud ice mixing ratio, (e) specific humidity, (f) relative humidity, (g) relative humidity due to changes in specific humidity and (h) relative humidity due to changes in temperature averaged over the tropical lands, tropical ocean, tropical deserts and tropical non-deserts between the 2xCO_2 and control experiments.

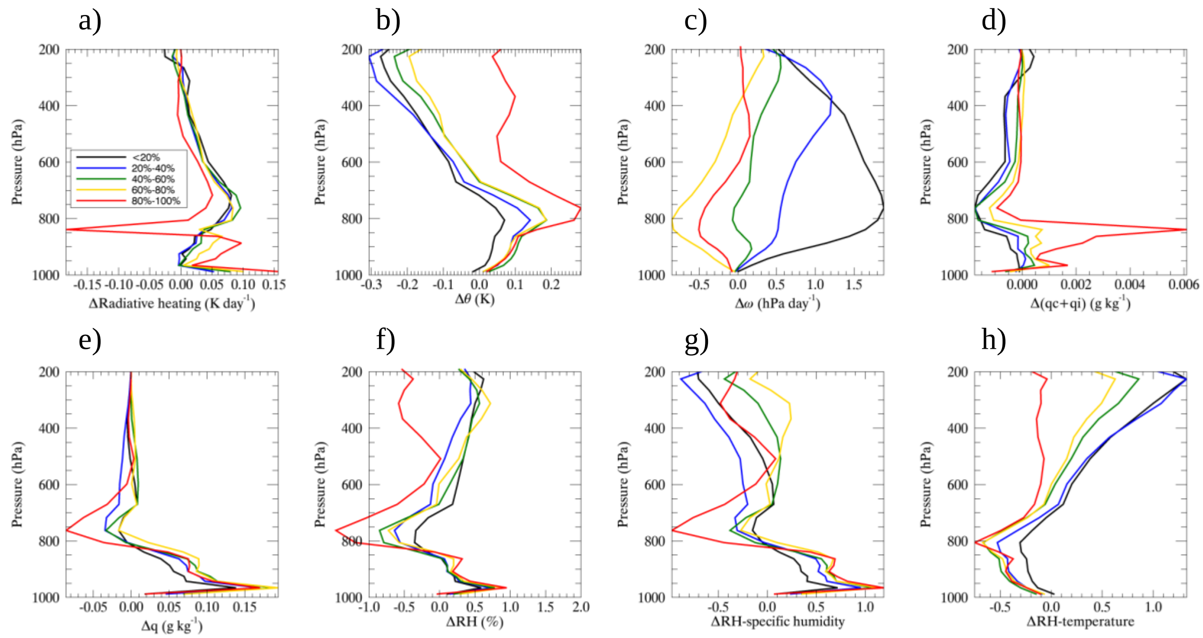

Figure 10. Same as Figure 9 except for the tropical ocean profiles sorted by annual-mean ω_{500}, each color represents the average for 20% of ω_{500} values. The 20%, 40%, 60% and 80% thresholds of ω_{500} are roughly -24 hPa, -1 hPa, 15 hPa, and 23 hPa.